Journal of Zhejiang University-SCIENCE A (Applied Physics & Engineering) 2022 23(1):68-82
www.jzus.zju.edu.cn; www.springer.com/journal/11582
E-mail: jzus_a@zju.edu.cn

Research Article

https://doi.org/10.1631/jzus.A2100135

Effects of the outlet pressure on two-phase slug flow distribution uniformity in a multi-branch microchannel

Peng-fei ZHANG[1], Xiang-guo XU[1,2], Yong-jun HUA[1], Yu-qi HUANG[1,3]✉

[1]*Department of Energy Engineering, Zhejiang University, Hangzhou 310027, China*
[2]*Center for Balance Architecture, Zhejiang University, Hangzhou 310027, China*
[3]*State Key Laboratory of Clean Energy Utilization, Department of Energy Engineering, Zhejiang University, Hangzhou 310027, China*

Abstract: The two-phase flow maldistribution phenomenon in microchannels with multi-parallel branches is inevitable in almost all common conditions, and not only affects the performance of the facility but also increases the risk of system instability. In order to better understand the distribution mechanism and to explore a potential strategy to improve uniformity, the pressure evolutions under different split modes in a microchannel with multi-parallel branches, were analyzed numerically. The results show that the fluctuations of transient pressure exhibit similar trends at various split modes, but the time-averaged pressure drops in the branches are very different. This may be related to the maldistribution of mass flow. Thus, the outlet pressures of the branches are numerically changed to explore the relationship between differential pressure and flow distribution. From this study, the flow distribution is seen to display a strong sensitivity to the branch differential pressure. By changing the pressure conditions, the gas flow of the middle branch can be effectively prevented from the main channel, and the flow type in this branch turns from gas-liquid to a single liquid phase. When the differential pressure of the first branch channel changes, the maldistribution phenomenon of the model can be mitigated to a certain extent. Based on this, by adjusting the differential pressures of the second branch, the maldistribution phenomenon can be further mitigated, and the normalized standard deviation (NSTD) decreases from 0.52 to approximately 0.26. The results and conclusions are useful in understanding the two-phase flow distribution mechanism and for seeking optimizing strategies.

Key words: Two-phase flow; Multi-parallel microchannel; Flow distribution; Slug flow; Split modes

1 Introduction

Because of trends in equipment miniaturization, the requirements of heat dissipation performance are significantly increased. Among many devices that enhance heat transfer, microchannel heat exchangers have always been favored by researchers for their unique advantages such as large specific surface area, high heat transfer coefficient, and low refrigerant flow requirement (Hong et al., 2018). At the same time, with the development of the new-energy vehicle industry and in order to meet the increasingly stringent requirements for thermal management of power batteries, some researchers have applied microchannel heat exchangers to direct refrigerant two-phase cooling systems for electric vehicle power batteries. Meinert et al. (2015) conducted a study on the refrigerant direct cooling system used on the BMW X5, and showed that the use of microchannel heat exchangers can provide 2 kW of cooling capacity for the battery while reducing energy consumption and weight. Hong et al. (2020) used experiments to compare liquid cooling and direct cooling of the battery using a refrigerant microchannel cold plate, and showed that the use of microchannel direct cooling can reduce the weight of the cooling system by 56% and achieve higher heat transfer efficiency and improved temperature control effect.

Although the heat exchange performance of the microchannel is outstanding, there are also problems such as large flow resistance, maldistribution, and blockage of the channel, which in turn cause instability of

✉ Yu-qi HUANG, huangyuqi@zju.edu.cn
Peng-fei ZHANG, https://orcid.org/0000-0001-5718-8399
Yu-qi HUANG, https://orcid.org/0000-0003-3152-5021

Received Mar. 30, 2021; Revision accepted July 5, 2021;
Crosschecked Nov. 26, 2021

the heat exchanger (Liang et al., 2010). Among many instability factors, the maldistribution phenomenon is widespread. Maldistribution in multi-microchannels will severely reduce the effectiveness of heat exchangers, even leading to mechanical failure of the devices and hydraulic instabilities (Dario et al., 2013). Therefore, the distribution mechanism of two-phase flow in microchannels is attracted increasing attention.

Analysis of previous research shows that the main factors affecting the maldistribution phenomenon include geometric structures, fluid properties, and operating conditions (Liu et al., 2017a; Zhou et al., 2017; Redo et al., 2019). Many researchers optimized the cross section shape (Tonomura et al., 2004), branch spacing (Liu and Wang, 2019), number of channels, different refrigerant flow paths (Bao, 2019), microchannel-header arrangements (Dario et al., 2015), and orientations (Liu et al., 2017b) to reduce the negative effects of maldistribution. Some researchers have used special geometric structures such as a tree-shaped distributor (Guo et al., 2020), protrusion configurations (Kim and Han, 2008; Marchitto et al., 2016), U-type configurations (Madanan et al., 2018), and a honeycomb type with single-sided expansion configurations (Nie et al., 2020) to restrain maldistribution phenomena. Moreover, the physical properties of the working fluid, such as density (Chen et al., 2012), viscosity (Zou and Hrnjak, 2014), wettability (Li et al., 2017), and surface tension (He et al., 2011) will affect the flow distribution of the microchannel heat exchanger.

It can be seen that traditional research on microchannel heat exchangers often requires a lot of experiments and data support. Numerous influencing factors and the complexity of two-phase flow have caused obvious differences between different experimental results. The versatility of the experimental results is low. The two-phase flow mechanism and the phase separation mechanism in the microchannel heat exchanger have not yet been unified. In view of this some researchers have tried to use numerical models to predict the flow distribution in the microchannel and make a reasonable explanation for the flow mechanism in the channel. Lee and Jeong (2019) developed a numerical analysis model to predict the quality distribution of two-phase flow in the header and the mass flow rate distribution in the branch channels. Mahvi and Garimella (2019a) proposed a new liquid distribution model for refrigerant flows in microchannel heat exchanger headers. Giannetti et al. (2020) developed a method to predict two-phase flow distribution in microchannel heat exchangers using an artificial neural network. These numerical models all use channel pressure change to predict the flow distribution in the microchannels.

For the phase separation mechanism, the computational fluid dynamics (CFD) method is widely used (Wang et al., 2014; Kumar et al., 2017). Three typical split modes according to the gas bubble length and flow ratio were identified by Kim and Lee (2015) and they proposed that shorter bubbles would induce more pronounced maldistribution. Dong et al. (2018) denoted two typical split modes according to gas bubble length and flow ratio. They pointed out that for the obstructing mode, the dominant driving force for phase split was upstream pressure. From these studies, the pressure was shown to be a key indicator inextricably linked with the flow distributions. The pressure drop affected by flow pattern and split models has been extensively studied. However, the aforementioned research on the phase separation mechanism is based on a T-junction. The phase separation process of multi-microchannels is rarely mentioned. Therefore, this paper attempts to study the phase separation mechanism of multi-microchannels from the perspective of the pressure drop, and proposes an optimization method for the maldistribution phenomenon.

In this study, a 3D model with multi-branches is established to simulate the two-phase flow distribution in parallel microchannels, and this numerical method is verified by experimental results. At the same time, this paper analyzes the pressure changes in different gas slug split modes, and achieves the goal of even flow distribution by changing the differential pressure of each branch channel. The results and conclusions are helpful for understanding the mechanism of two-phase flow and establishing a universal two-phase flow distribution prediction model.

2 Numerical methodology

The numerical studies were performed by using the interFlowRate solver. This solver was developed based on an interFlow solver, an open-source CFD code named OpenFOAM (Ver. 6.0). This solver is

based on the volume of fluid (VOF) method and the isoAdvector method to reconstruct the interface of two fluids. The VOF method has been widely used in the study of slug flow (Bordbar et al., 2018; Ferrari et al., 2018; Yu et al., 2019). The isoAdvector method is a new VOF-based interface advection method developed by Roenby et al. (2016). The traditional two-phase flow model in OpenFOAM uses the multi-dimensional universal limiter for explicit solution (MULES) method for interface reconstruction, which is an algebraic reconstruction method. The basic theory of the MULES method is the flux corrected transport (FCT) technique. Compared with the MULES method, the isoAdvector method has unique advantages in tracing the sharp interface and offers improved algorithm robustness even on unstructured meshes. It has the same accuracy as the geometric reconstruction schemes. The details of the numerical approach are explained in the following section.

2.1 Governing equations

As the evolution of bubbles keeps changing with time, especially at the junctions of the main channel and the branch channels, the transient equations should be solved. The continuity and the momentum equations are given as follows:

$$\frac{\partial \rho}{\partial t}+\nabla\cdot(\rho\boldsymbol{u})=0, \tag{1}$$

$$\frac{\partial(\rho\boldsymbol{u})}{\partial t}+\nabla\cdot(\rho\boldsymbol{u}\boldsymbol{u})=-\nabla p+\nabla\cdot\left[\mu(\nabla\boldsymbol{u}+\nabla\boldsymbol{u}^{\mathrm{T}})\right]+\rho\boldsymbol{g}+\boldsymbol{F}_{\mathrm{s}}, \tag{2}$$

where ρ is the density of the fluid, $\boldsymbol{u}$ is the velocity, t is the time, p is the pressure, $\boldsymbol{g}$ is the gravity acceleration, μ is the dynamic viscosity, and $\boldsymbol{F}_{\mathrm{s}}$ is the interfacial tension force which can be calculated by the continuum surface force (CSF) model:

$$\boldsymbol{F}_{\mathrm{s}}=\sigma\kappa\nabla\alpha=\sigma\left[\nabla\cdot(\nabla\alpha/|\nabla\alpha|)\right]\nabla\alpha, \tag{3}$$

where σ is the surface tension coefficient, κ is the interface curvature, and $\nabla\alpha$ is the vector normal to the interface.

The VOF method is used to trace the location of the interface between two fluids. The volume fraction (α) is an indicator function to distinguish different fluids. It can be obtained by

$$\frac{\partial\alpha}{\partial t}+\nabla\cdot(\boldsymbol{u}\alpha)=0, \tag{4}$$

where α=0 represents the gas phase, α=1 represents the liquid phase, and 0<α<1 represents the interface between two phases. According to the definition of the volume fraction, the density and the viscosity in the interface region can be expressed as follows:

$$\rho=\alpha\rho_{\mathrm{l}}+(1-\alpha)\rho_{\mathrm{g}}, \tag{5}$$

$$\mu=\alpha\mu_{\mathrm{l}}+(1-\alpha)\mu_{\mathrm{g}}, \tag{6}$$

where the indices l and g represent the liquid phase and the gas phase, respectively.

Using the finite volume method (FVM), the α equation is discretized as follows:

$$\alpha(t+\Delta t)=\alpha(t)-\frac{\sum_{\mathrm{f}}\Delta V_{\mathrm{f}}(t,\Delta t)}{V}=\alpha(t)-\frac{\sum_{\mathrm{f}}\int\boldsymbol{u}_{\mathrm{f}}\cdot\alpha_{\mathrm{f}}S_{\mathrm{f}}\mathrm{d}t}{V}, \tag{7}$$

where the subscript f represents the physical quantity of the mesh surface center, and α_{f}, $\boldsymbol{u}_{\mathrm{f}}$, and S_{f} represent the volume fraction, velocity, and area of the mesh surface center, respectively. V represents the volume of the mesh cell, and $\Delta V_{\mathrm{f}}(t, \Delta t)$ represents the change of the fluid volume in the mesh face.

In order to improve the accuracy of the α equation, the isoAdvector method uses more precise processing which rewrites the above equation as follows (Roenby et al., 2016):

$$\Delta V_{\mathrm{f}}(t,\Delta t)=\boldsymbol{u}_{\mathrm{f}}\cdot\int A_{\mathrm{f}}\mathrm{d}t, \tag{8}$$

where A_{f}=$\alpha_{\mathrm{f}}S_{\mathrm{f}}$ and A_{f} represents the area occupied by the fluid on the mesh surface.

2.2 Numerical model and boundary conditions

Liu et al. (2017a) experimentally studied the phase distribution of two-phase slug flow in three parallel microchannels under different inlet flow conditions. In their study all the channels have square cross-sections. The sizes of the main channel and branch channel are 1 mm×0.5 mm and 0.5 mm×0.5 mm, respectively. The length between the center of two branch channels is 12 mm. There is also a buffer flow zone

of 1 mm at the end of the main channel. The numerical model used in this paper is shown in Fig. 1, which is consistent with these sizes. The model has three branches, and the gas bubble is generated from the inlet boundary and will split successively at the two T-junctions. The inlet volume flow rate is Q_1 which can be calculated by adding the inlet gas volume flow rate Q_{1g} and the inlet liquid volume flow rate Q_{1f}. The outlet volume flow rates are Q_2, Q_3, and Q_4, respectively.

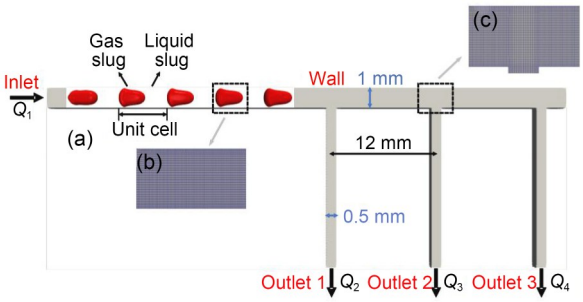

Fig. 1 Computational domain used in simulations: (a) geometry and boundary; (b) mesh of main channel; (c) mesh of T-junction

A structured mesh was used to divide the computing domains. In order to capture the liquid film around the gas slug, it is necessary to refine the mesh near the wall. As shown in Fig. 2, the mesh independence test was conducted with the boundary layer minimum cell size, ranging from 0.016 mm to 0.05 mm. The liquid film thickness around the gas bubble was increased by decreasing the minimum cell size of the boundary layer, which was almost unchanged with the boundary layer cell size below 0.02 mm. The y+ value of this cell size is 0.634 684, which meets the requirements of the boundary layer calculation. Thus, a boundary layer minimum cell size of 0.02 mm was selected to generate the structured mesh. The cross sections of the main channel and the branch channel were divided into 522 and 324 meshes, respectively. To improve calculation accuracy, the meshes were compressed gradually from the center of the channel to the wall. The total number of the meshes in this study is 1.6 million. The maximum aspect ratio is 3.401 36. The maximum non-orthogonality is 5.781 85 and the maximum skewness is 0.087 052 2. The quality of all the meshes meets those requirements.

In this study, transient, periodic inlet, and boundary conditions are used to generate the inlet slug flow. Asadolahi et al. (2011) developed a method to achieve

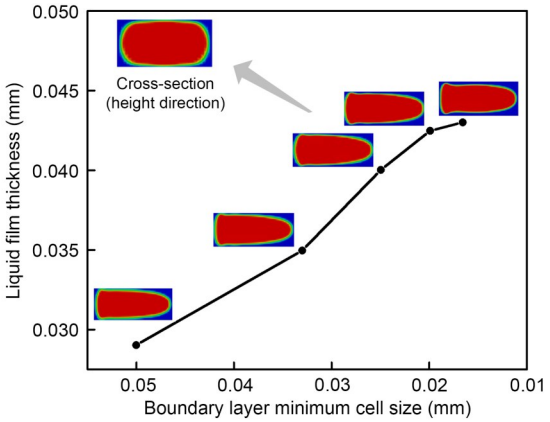

Fig. 2 Mesh independence test

this. As shown in Fig. 3, there are two processes for the inlet boundary. First, the inlet surface is full of liquid and then the gas slug with a thin liquid film enters the main channel from the inlet surface. These processes occur periodically over the simulation time. The velocity at the inlet boundary is set to be constant. Thus, the total time of an unit cell t_{UC} can be divided into two parts:

$$t_{UC} = t_g + t_f, \tag{9}$$

where t_f represents the time of the first process and t_g represents the time of the second process. t_g can be calculated by the gas bubble volume, which can be expressed as follows (Kim and Lee, 2015):

$$V_g = S_g\left(L_g + L_f\right)\cdot\frac{j_g}{u_b}, \tag{10}$$

where L_g is the length of gas bubble, L_f is the length of the liquid slug, j_g is the superficial velocity of the gas, u_b is the velocity of the gas bubble, and S_g is the area of gas at the inlet surface. It is necessary to undertake preliminary simulations to obtain the length of the liquid film around the gas bubble and, based on that value, S_g can be determined.

The relation between t_g and V_g can be expressed as follows:

$$u_{inlet}\cdot S_g\cdot t_g = V_g, \tag{11}$$

where u_{inlet} is the total superficial velocity at the inlet. t_f can be obtained by the length of the liquid slug:

$$t_{\mathrm{f}}=\frac{L_{\mathrm{f}}}{u_{\mathrm{inlet}}}. \tag{12}$$

To create multiple bubbles, a non-dimensional number R_{t} is created as follows:

$$R_{\mathrm{initial}}=\frac{t_{\mathrm{f}}}{t_{\mathrm{UC}}}, \tag{13}$$

$$R_{\mathrm{t}}=\frac{t}{t_{\mathrm{UC}}}-\mathrm{int}\left(\frac{t}{t_{\mathrm{UC}}}\right), \tag{14}$$

where t is the simulation time. The function int can return the integer part of its argument. Based on this, the two processes described above can be expressed as

$$\begin{cases}0<R_{\mathrm{t}}<R_{\mathrm{initial}}, & \text{liquid slug entry,}\\ R_{\mathrm{initial}}<R_{\mathrm{t}}<1, & \text{gas bubble entry.}\end{cases} \tag{15}$$

For the outlet boundary conditions, the volume flow rates through outlet 1 and outlet 2 were set to be constant at Q_2 and Q_3, respectively. The corresponding pressure boundary condition is fixed in FluxPressure which can adjust the pressure gradient to fit the velocity boundary condition. As for outlet 3, a pressure outlet boundary condition is used. Moreover, a no-slip boundary condition is set at all the channel walls and the constant contact angle (θ=30°) is imposed. In order to obtain the result for the full-developed state, the length of the main channel should be of sufficient length. At the initialization process, all computation domains are full of fluid. In order to calculate the average flow rate, it is necessary to save the data of the instantaneous flow rate during the simulation process. Based on interFlow solver, the interFlowRate solver embeds the code of instantaneous flow rate calculation and output data to the file over time. The total flow rate can be obtained by adding all flux (e.g. parameter phi in the solver code) on the sample surface. Moreover, the flow rates of liquid and gas are calculated by multiplying the volume fraction with the total flow rate. In this study, 0.03% (in weight) sodium dodecyl sulfate (SDS) solution and nitrogen were chosen to be the liquid phase and the gas phase, respectively. The physical properties are as shown in Table 1.

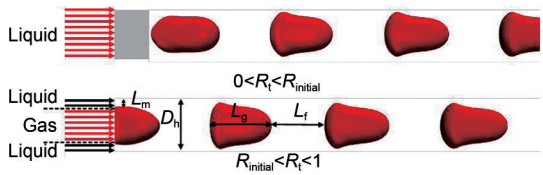

Fig. 3 Periodic inlet boundary conditions

2.3 Numerical scheme

The governing equations were discretized through the FVM method. The pressure-implicit with splitting of operators (PISO) algorithm was used to couple the pressure and velocity. Finally, the volume fraction of each phase in the computational nodes was calculated. The discretization of the convection terms in the momentum equations and α equation were performed using the Gauss up-wind scheme and the Gauss van Leer scheme. The discretization of the grad terms was performed using the Gauss linear scheme.

In order to ensure computational convergence, the adaptive time-step was used to maintain the value of the maximum Courant number below 0.8. Adaptive time-step is an algorithm that can modify the time-step during the simulation process. Compared with the fixed time-step algorithm, this algorithm can reduce the simulation time while ensuring the Courant number meets the requirements of users. At the same time, MATLAB was used to post-process the data in the file which was output by the interFlowRate solver. Thus, the average flow rate, average pressure, and split ratio can be obtained.

3 Results and discussion

3.1 Model validation

The test experimental data is taken from case A-$L_{\mathrm{GS}}/D_{\mathrm{h}}$=2.05 and case C-$L_{\mathrm{GS}}/D_{\mathrm{h}}$=0.95 in Liu et al. (2017a)'s research (where $L_{\mathrm{GS}}/D_{\mathrm{h}}$ represents the ratio of the length of the gas slug to the hydraulic diameter of the microchannel header). The flow rate of the outlet is calculated by the relation between the phases split

Table 1 Physical properties of fluids used in the study

Fluid	Density, ρ (kg/m^3)	Viscosity, μ (mPa·s)	Surface tension, σ (mN/m)
SDS solution (0.03%, in weight)	997.35	0.8670	29.2
Nitrogen	1.25	0.0178	29.2

ratio and the phases inlet flow rate. By calculating the Bond number, Reynolds number, Capillary number, and Weber number, the flow can be confirmed to be laminar and the influence of gravity can be ignored.

Fig. 4 compares the experimental pictures taken from Liu et al. (2017a) with the cloud maps of liquid volume fraction by simulation. The visualized slug flow and distributions are displayed in Figs. 4a and 4b, respectively, where the upper pictures are taken from Liu et al. (2017a), and the contours of liquid volume fraction displayed at the bottom are calculated by the simulation in this study. The simulated gas slug lengths display obvious similarity with experiments, whether before or after the splitting, at all these three conditions. Some feature zones are extracted from Fig. 4a, where m_1, m_2, and m_3 represent different regions in the main channel, and b_1, b_2, and b_3 represent the regions in various branches. Comparing the length ratios of gas bubble to liquid slug at all these six feature points, the simulation results and experimental results have very similar trends. This indicates that the simulation model is credible for analyzing the two-phase flow distribution in multi-branches.

3.2 Transient pressure evolution and split modes

For the convenience of analysis, the parallel microchannels with three branch channels can be regarded as two T-junctions connected: T-junction 1 and T-junction 2 from left to right. As shown in Fig. 4, different split modes are presented under different

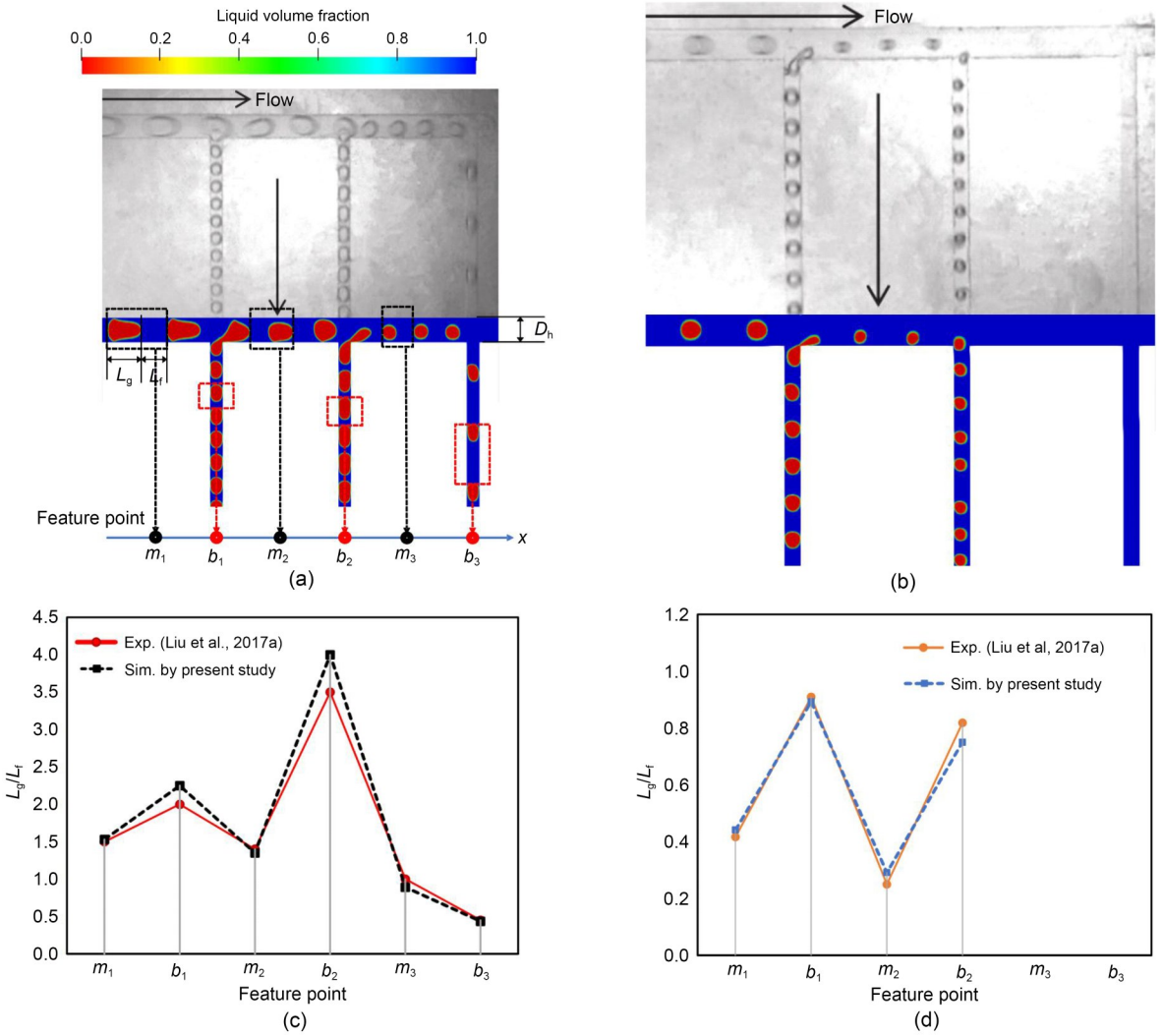

Fig. 4 Comparison of the experimental results (Liu et al., 2017a) against numerical simulations in the present study. The visualized slug flow and distributions are displayed in case A-L_{GS}/D_h=2.05 (a) and case C-L_{GS}/D_h=0.95 (b). The length ratios of gas bubble to liquid slug at different feature points are plotted in case A-L_{GS}/D_h=2.05 (c) and case C-L_{GS}/D_h=0.95 (d)

simulation conditions. In case A-L_{GS}/D_h=2.05, the split modes of T-junction 1 and T-junction 2 belong to the breakup with part obstruction (B_2) modes. In case C-L_{GS}/D_h=0.95, the split modes of T-junction 1 belong to the breakup with permanent tunnel (B_3) and T-junction 2 belongs to the non-breakup/branch-flow (NB/B). In case A-L_{GS}/D_h=3.46 (Fig. 5), all T-junctions belong to the breakup with permanent obstruction (B_1) mode. Here, all split modes are reported by Wang et al. (2014) and Ménétrier-Deremble and Tabeling (2006).

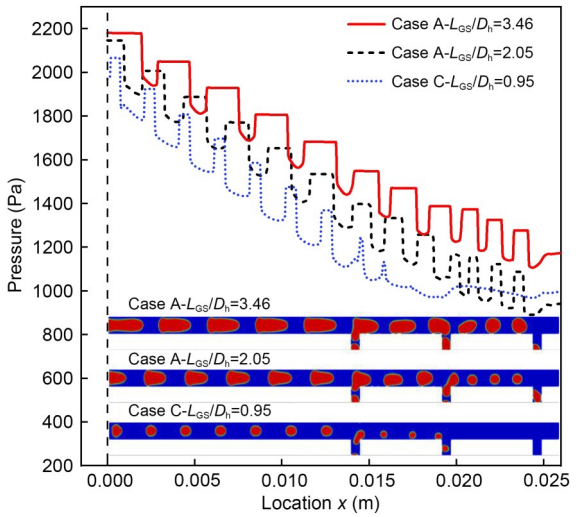

Fig. 5 Pressure evolution in the main channel

Fig. 5 shows the pressure change curve on the central axis of the main channel. It can be seen that the main channel presents a typical slug flow pressure drop. The entire graph can be divided into three parts based on the branch channels. Each time the slug bubble passes through a branch channel, the pressure drop rate for the liquid phase in the main channel will decrease. This can be derived from the difference between the adjacent lowest pressure points of the pressure curve in the figure. Each time the slug bubble passes through a branch channel, the difference between the adjacent lowest pressure points is significantly reduced. As shown in Fig. 6a, in order to facilitate the analysis, one cycle data is selected for processing. The data point selection is the geometrical abrupt position of the branch channel. For branch channel 1, there is a sudden increase in pressure at 7.418×10^{-2} s. This is mainly because the gas slug blocks both the main channel and the branch channel, which leads to an increased resistance to flow of the continuous fluid. It is worth noting that the thickness of the liquid film between the gas

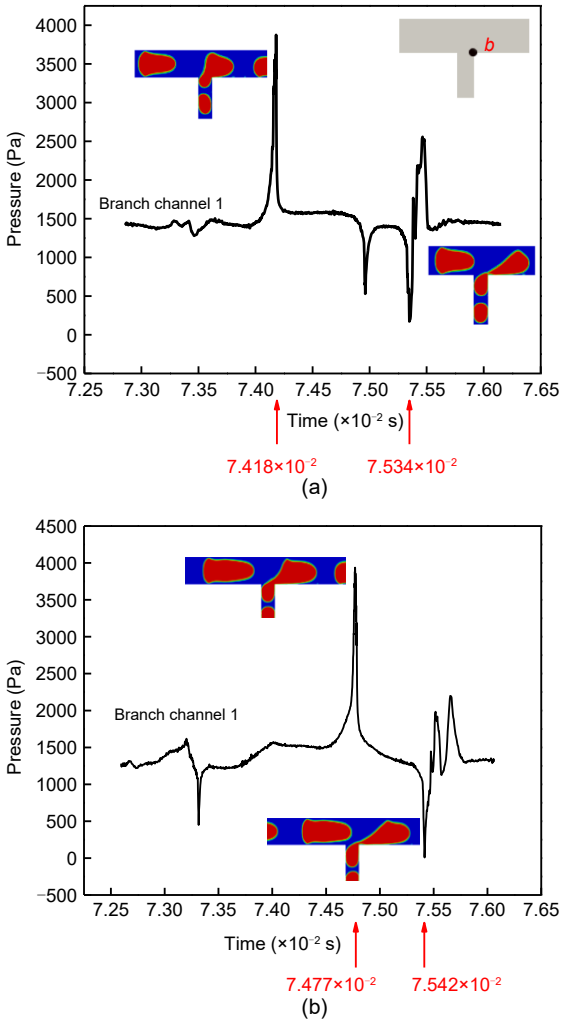

Fig. 6 Evolution of the static pressures in one cycle: (a) case A-L_{GS}/D_h=2.05; (b) case A-L_{GS}/D_h=3.46

slug and the wall in the main channel reaches a minimum value at this time. At the same time, due to the increased pressure of the continuous fluid, the neck which connects the daughter bubble in the branch channel to that in the main channel becomes thinner. Subsequently, due to the stretching of the neck, the thickness of the liquid film in the main channel gradually increases and the pressure drops. This is consistent with the pressure change process observed by Singh et al. (2020). The only difference between that and this study is the gradient of pressure change. The reason is that the dispersed phase is gas and the continuous phase is liquid in this study. The density of these two phases is quite different whilst in Singh et al. (2020)'s experiment, both the dispersed phase and the continuous phase are liquid.

There is a significant pressure drop at the moment when the neck of gas slug breaks. The reason for this is mainly related to the surface tension, according to the Laplace pressure calculation formula, $\Delta p_L=\gamma(r_a^{-1}+r_r^{-1})$, where r_a is the axial curvature, r_r is the radius of the radial curvature, and γ is the surface tension coefficient. At this time, the radial curvature tends to infinity, so the Laplace pressure is quite large. The large gas-liquid differential pressure causes a sudden pressure change. Conversely, the pressure will have a small fluctuation because of the influence of the downstream branch channel. With the generation of the daughter bubbles, the pressure in the channel recovers.

As shown in Fig. 6b, for case A-L_{GS}/D_h=3.46, the general law of pressure evolution is similar to the case A-L_{GS}/D_h=2.05. At 7.477×10^{-2} s, the gas slug blocks the main channel which causes a pressure increase. At 7.542×10^{-2} s, the gas slug breaks which leads to a sudden drop in pressure and an obvious pressure fluctuation. It can be seen from the above analysis that the pressure will appear as a unique crest and trough in the process of the gas slug break, which corresponds to different break phases. The crest corresponds to the pressure increase caused by the gas slug blocking the main channel. The trough corresponds to the moment when the gas slug breaks into two daughter bubbles. Due to the breaking of the gas slug, the pressure in the microchannel will fluctuate significantly.

For case C-L_{GS}/D_h=0.95, the pressure evolution law is obviously different from the previous two cases. As shown in Fig. 7a, for branch channel 1, there is no sudden increase in pressure. The reason is that, for the B_3 mode, there is no block phenomena in the main channel during the gas slug split process. The flow resistance of the continuous fluid does not change significantly, so the pressure evolution is relatively stable. Similar to the aforementioned modes, the pressure suddenly decreases at the moment the gas slug breaks. However, the pressure evolution change process of branch channel 2 (NB/B) does not show any of the aforementioned phenomena. When a gas bubble enters branch channel 2, the flow resistance in this branch channel increases, causing the pressure upstream of the gas bubble in this channel to be maintained at a low level. Therefore, the pressure at Point *a* drops significantly. At 8.951×10^{-2} s, the next bubble moves to Point *a*. At this time, the pressure at Point *a* represents the internal pressure of the bubble, that is, the pressure rises sharply. Compared with Point *a*, the pressure at Point *b* has been maintained at a higher level. It can be observed from the vector graph in Fig. 8. When the fluid enters into the branch channel from the main channel, more fluid tends to enter the branch channel from the side of Point *b* due to the inertia of the fluid. This causes the fluid velocity at Point *b* to be higher than the fluid velocity at Point *a*, resulting in an obvious vortex at the inlet of the branch channel. Therefore, the vortex area in the branch channel (Point *a*) shows a lower pressure, while Point *b*, which is impacted by more continuous fluid, shows a higher pressure.

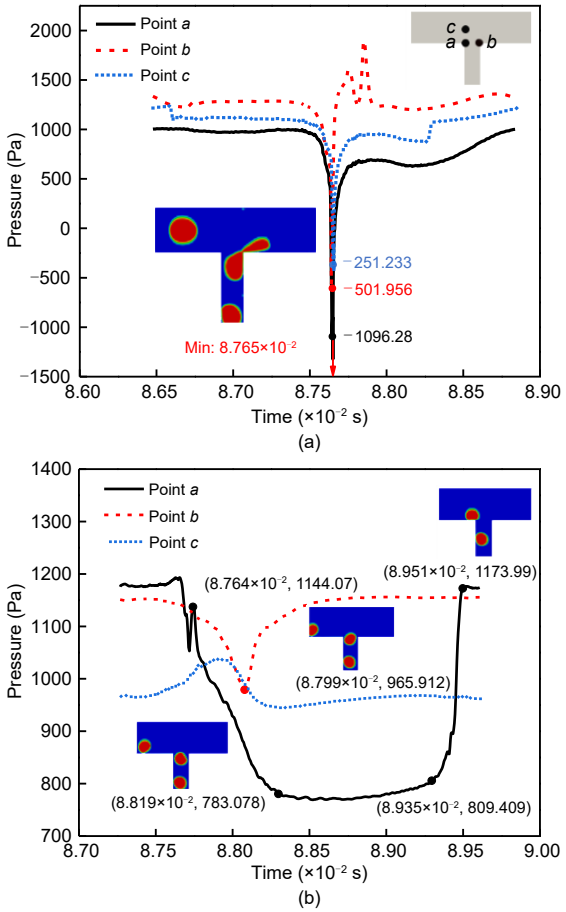

Fig. 7 Evolution of the static pressure of case C-L_{GS}/D_h=0.95: (a) branch channel 1; (b) branch channel 2

From these studies, it can be observed that the pressure changes of different split modes have similarities and differences. For all split modes with bubble break (e.g. B_1 mode, B_2 mode, and B_3 mode), when the gas slug is about to break into daughter bubbles, the pressure in the channel drops sharply and obvious

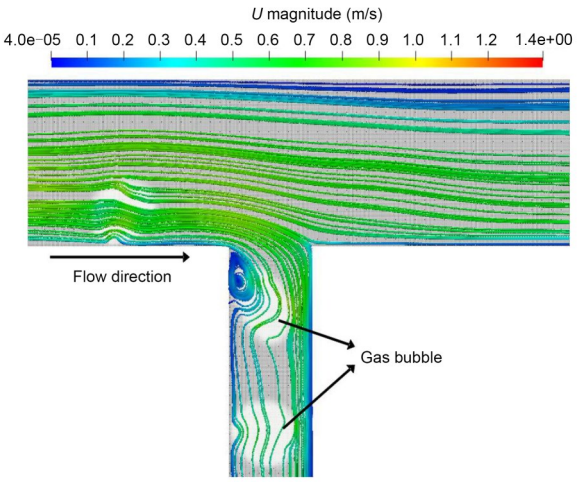

Fig. 8 Vector graph of branch channel 2 (*U*: velocity)

fluctuations appear. For the B_1 and B_2 modes, the gas slug is longer, which will block the channel during the split process and cause the pressure to increase. Conversely, the B_3 mode does not experience this phenomenon. For the NB/B mode, the pressure changes show obvious differences. Due to the mutual coupling between different branch channels, the pressure change of one branch channel will be reflected to other branch channels at the same time. This also further demonstrates that the pressure distribution of the branch channel is inseparable from the flow distribution of the microchannel, which provides a possible optimizing method for multi-branch distribution.

3.3 Time-averaged pressure drop and flow distribution

In order to study further the relationship between pressure and flow distribution, the time-averaged pressure drop of each branch channel flow path was calculated based on the plane M, as shown in Fig. 9a. Taking flow path MC as an example, the total pressure drop includes the pressure drop of two parts of slug flow in the main channel between plane M and the crossing of branch channel 3 (ΔP-header), the pressure drop at the crossings of three branch channels (ΔP-crossing), and the pressure drop of slug flow in branch channel 3 (ΔP-branch). It can be seen from Figs. 9b and 9c that the pressure drop of the branch channels dominates, and the flow distribution of the microchannel is closely related to the pressure drop in each branch channel. For flow path MA, as the length of the gas slug in the main channel decreases, the corresponding pressure drop at

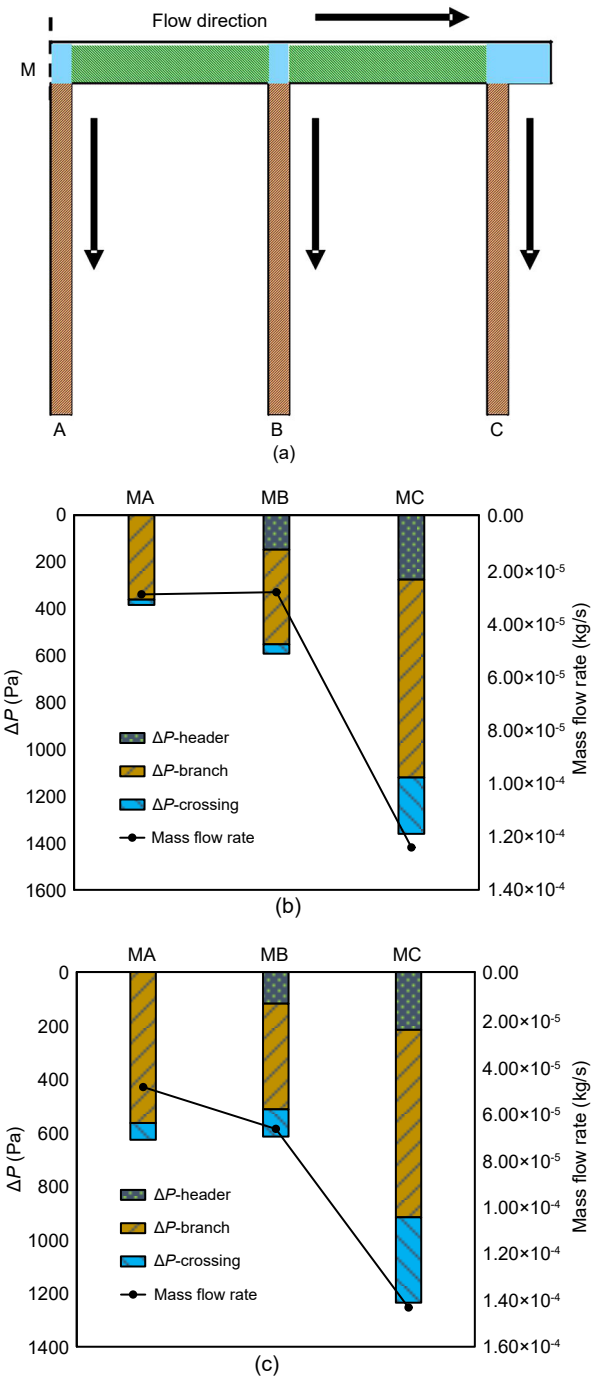

Fig. 9 Schematic diagram of pressure drop and mass flow rate distribution in microchannels: (a) scheme of the flow path diagram; (b) case A-L_{GS}/D_h=2.05; (c) case C-L_{GS}/D_h=0.95

the branch channel 1 crossing increases gradually. The main reason is that the longer the gas slug length, the closer it is the single-phase flow during the splitting process which means that the pressure drop is relatively small. In flow path MC, the pressure drop of

the crossing of branch channel 3 is large. This might be because the end of the main channel is closed which leads to a vortex structure there.

From Fig. 9, it can be observed that the pressure drops in branches are very different. Meanwhile the mass flow rates in branches are also different, and show similar trends to the pressure drops. This indicates that the pressure characteristics may be closely related to the flow distribution. Both pressure drop and mass flow rate in branch 3 are the greatest, with a large difference from the second greatest one. In Fig. 9b, the mass flow rate in branch channel 3 is even greater than those in branch channels 1 and 2. Thus, the direction of optimization is to increase the mass flow rate in branch channels 1 and 2. By adjusting the outlet pressure of the upstream two branches properly, the flow distribution may be changed effectively. Therefore, the following discussion is about the effects of changing the outlet pressures of the branches.

3.4 Optimization scheme

The two-phase flow distribution can be specified by the mass flow rates of each branch channel. In this study, the average mass flow rate in the branch channel is derived from simulation data processing. In order to compare the maldistribution of the microchannel heat exchanger under different working conditions, the average mass flow rate needs to be normalized. The normalization process is as follows:

$$\dot{m}_j^*[i]=\frac{\dot{m}_j[i]}{\left(\sum_{i=1}^{N_{ch}}\dot{m}_j[i]\right)\Big/N_{ch}}, \tag{15}$$

where i denotes the branch channel number, $\dot{m}$ is the mass flow rate, j specifies the phase (l represents liquid, g represents gas, and t represents total), and N_{ch} is the total number of branch channels (N_{ch}=3 in this study). $\dot{m}^*$ is the non-dimensional mass flow rate in a given branch channel.

The normalized standard deviation (NSTD) is defined in Eq. (16). This parameter is the ratio of the standard deviation of the branch channel mass flow rates to the maximum possible standard deviation. The value range of NSTD is 0–1. An NSTD value close to 0 indicates a more even distribution. Conversely, an NSTD value close to 1 indicates a less even distribution (Mahvi and Garimella, 2019b).

$$\mathrm{NSTD}_j=\sqrt{\frac{\sum_{i=1}^{N_{ch}}\left(\dot{m}_j^*[i]-1\right)^2}{\left(N_{ch}-1\right)N_{ch}}}. \tag{16}$$

Compared with the liquid phase, the gas mass flow rate has an order of magnitude difference. Thus, the total mass flow rate is similar to the liquid mass flow rate, and the $\mathrm{NSTD_t}$ and $\mathrm{NSTD_l}$ are also similar. However, in the actual application process, the uniform liquid mass flow rate is beneficial to the uniform distribution of the temperature of the heat exchange equipment. Therefore, the subsequent analysis process mainly focuses on the uniformity of the liquid mass flow rate distribution. As shown in Table 2, the $\mathrm{NSTD_l}$ is greater than 0.5, and the liquid mass flow rate of branch channel 3 is always the greatest, even four time that of branch channel 1. Therefore, in order to reduce the maldistribution phenomenon, it is necessary to reduce the mass flow rate of the third branch channel. Pressure is often a very important parameter in affecting the mass flow distribution. The differential pressure distribution in different branch channels directly determines the mass flow distribution. However, the differential pressure cannot be directly controlled. Thus, in order to optimize the existing model, the differential pressure is indirectly changed by changing the outlet pressure of different branch channels. In the simulation, increasing the outlet pressure of one branch channel means that the differential pressure of this branch channel decreases. In practical applications, the purpose of controlling the differential pressure of different branch channels can be achieved by changing the diameter of the branch channels.

Table 2 Non-dimensional flow rate and $\mathrm{NSTD_l}$ (for case A-L_{GS}/D_h=2.05)

Branch	m^*
1	0.49
2	0.47
3	2.04
$\mathrm{NSTD_l}$	0.52

On the basis of the case A-L_{GS}/D_h=2.05, the pressure of branch channel 1 is reduced at interval of 50 Pa, and the mass flow distribution is as shown in Fig. 10a. The data corresponding to the solid circle in this figure is based on the experimental conditions of Liu et al. (2017a)'s research. As the differential pressure of branch channel 1 continues to increase,

the mass flow rate of this branch channel also increases. For branch channel 2 and branch channel 3, the direction of trend is opposite, and there is a turning point. When the differential pressure of branch channel 1 is lower than 487 Pa, the mass flow rates of branch channel 1 and branch channel 2 have little change. When the differential pressure of branch channel 1 is between 487 Pa and 531 Pa, with the increase of the differential pressure, the mass flow rate of branch channel 2 shows an increasing trend, while the mass flow rate of branch channel 3 shows a decreasing trend. This change trend makes the mass flow distribution in the microchannel tend to be uniform, that is, the value of $NSTD_l$ decreases (Fig. 10c). However, when the differential pressure of branch channel 1 is higher than 531 Pa, the flow change trend of branch channel 1 and branch channel 2 will turn. The mass flow rate of branch channel 2 gradually decreases and the mass flow rate of branch channel 3 gradually increases. This results in an increase in the flow difference of these three branch channels and the maldistribution is more obvious, that is, the value of $NSTD_l$ increases accordingly.

The main reason for the above phenomenon can be observed from the phase fraction contour (Fig. 10c). When the differential pressure of branch channel 1 is lower than 531 Pa, the flow regime of all three branch channels belongs to two-phase flow distribution. As the differential pressure of branch channel 1 increases gradually, it can be observed that more gas tends to enter branch channel 1. The gas phase in branch channel 2 decreases gradually until the gas phase completely disappears and branch channel 2 becomes a single-phase flow. For branch channel 3, the gas mass flow rate increases when branch channel 2 is two-phase flow. When branch channel 2 becomes single-phase flow, the gas mass flow rate of branch channel 3 decreases rapidly (Fig. 10b). The most intuitive explanation of this process is that the length of the gas slug in branch channel 1 is increasing in length, and the bubble size in the downstream part of the main channel gradually decreases. Based on the above analysis, before branch channel 2 becomes single-phase flow completely, due to the reduction of the gas phase ratio, the volume of the daughter bubble located in branch channel 2 is reduced during the split of the gas slug. Thus, the blocking effect on branch channel 2 is weakened, and the flow area of the liquid phase is

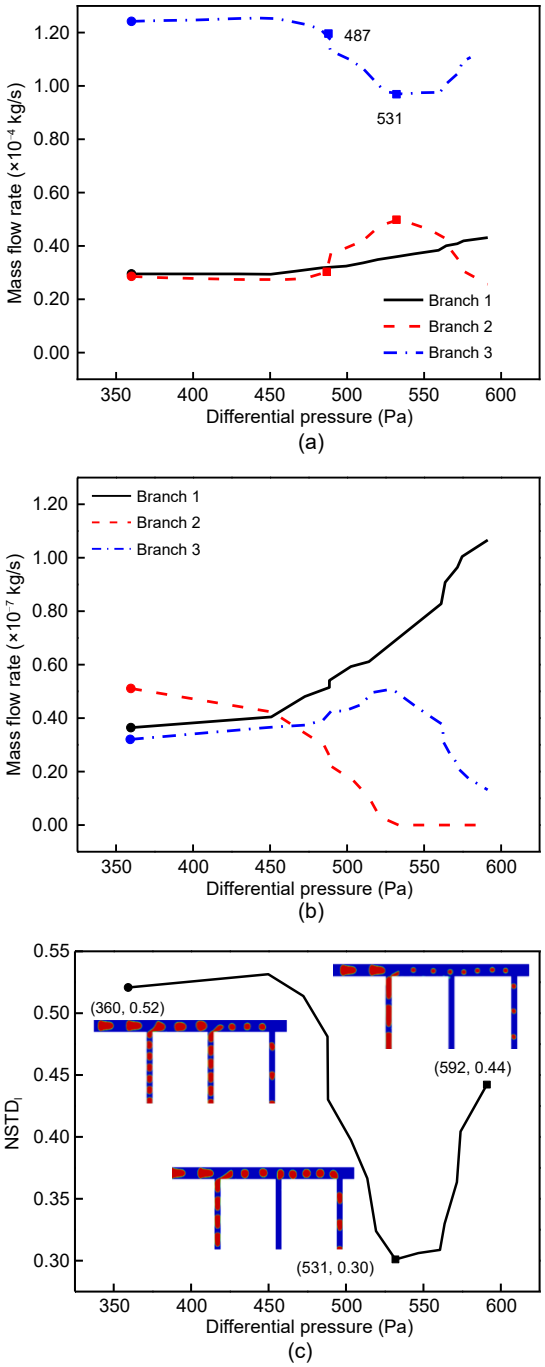

Fig. 10 Effects by changing the outlet pressure of branch channel 1: (a) liquid mass flow rate distribution; (b) gas mass flow rate distribution; (c) change of $NSTD_l$

increased. However, the special elongated bubble structure formed during the split of the gas slug will cause a significant vortex above the bubble, which will help the liquid phase flow into the branch channel. Under the combined action of these two, the liquid mass flow rate in branch channel 2 is increased. When

branch channel 2 is completely converted to single-phase flow, the elongated bubble structure disappears, and the bubbles in the main channel become significantly smaller. Thus, there is basically no blocking effect on the branch channel and main channel. As a result, due to the influence of fluid inertia, more liquid does not enter into branch channel 2, but tends to flow into branch channel 3. The liquid mass flow rate in branch channel 2 is decreased, and that in branch channel 3 is increased.

From the foregoing analysis, the following inferences can be made: (1) The change in differential pressure of branch channel 1 can reduce the $NSTD_l$ of the entire model significantly. However, because branch channel 2 becomes single-phase flow state prematurely, this reduction effect is limited to a certain extent. (2) Before the turning point, the influence of the differential pressure of branch channel 2 on the liquid phase mass flow rate of branch channel 1 and branch channel 3 is not obvious. Therefore, while changing the outlet pressure of branch channel 1, and changing the outlet pressure of branch channel 2 appropriately, branch channel 2 maintains two-phase flow which can further mitigate the maldistribution phenomenon of the entire model.

In order to verify the above hypothesis, the outlet pressure of branch channel 2 is reduced on the basis of the differential pressure of branch channel 1 being 531 Pa ($NSTD_l$=0.30). The simulation results are shown in Fig. 11 and the abscissa in this figure is the differential pressure of branch channel 2. It can be seen from Fig. 11b that there is a turning point in the optimization process of the $NSTD_l$. Before the turning point, the liquid phase mass flow rate of branch channel 2 increases as the differential pressure of branch channel 2 increases. At the same time, branch channel 2 changes gradually from single-phase flow to two-phase flow. The liquid phase mass flow rate of branch channel 3 is further reduced, while the liquid phase mass flow rate of branch channel 1 does not change significantly. Within this range, the $NSTD_l$ of the whole model is reduced from 0.30 to 0.26, and the maldistribution phenomenon is further optimized. After the turning point, if the differential pressure of branch channel 2 is increased continuously, the flow difference of these three branch channels will increase. The value of NSTD will also increase rapidly and the maldistribution phenomenon of the whole model will be more obvious. Therefore, the maldistribution phenomenon of the whole model can be significantly minimised by effectively controlling the differential pressure of the three branch channels.

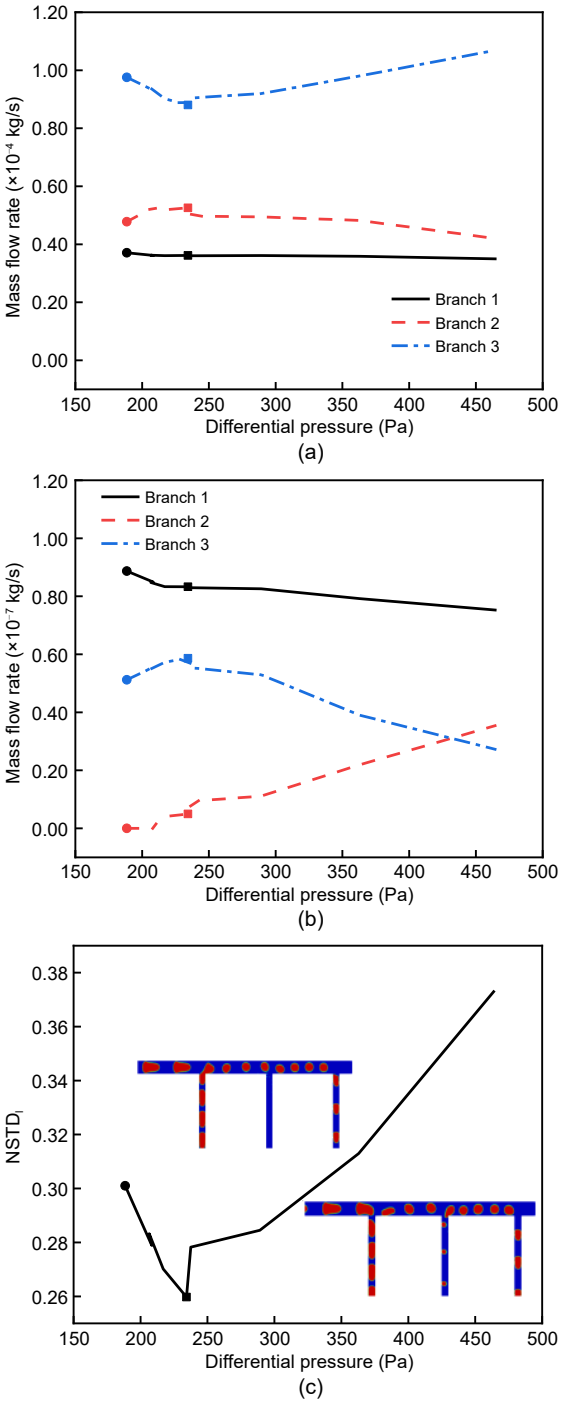

Fig. 11 Thermal equilibrium temperatures of the foundation material with different operating temperatures: (a) liquid mass flow rate distribution; (b) gas mass flow rate distribution; (c) change of $NSTD_l$

As shown in Fig. 12, through optimization, the flow rate distribution of the microchannel tends to be uniform by changing the outlet pressure of branch channels 1 and 2, and the value of $NSTD_l$ can be reduced from 0.52 to 0.26. In the actual application process, a similar effect can be achieved by changing the length, diameter or other geometric parameters of the branch channels. For example, three branch channels with different lengths or diameters, or even any number of branch channels, can be used to obtain the combination of different differential pressures and achieve the optimal distribution effect.

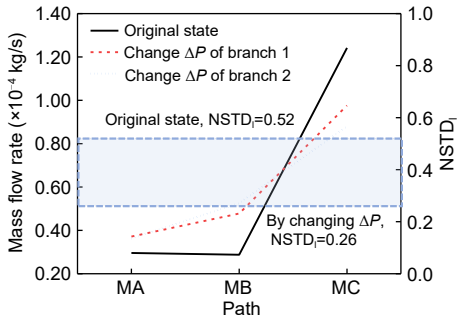

Fig. 12 Mass flow rate distributions at different conditions (ΔP: differential pressure)

4 Conclusions

A numerical method for the splitting process of two-phase flow in a microchannel with multi-parallel branches is developed to analyze the pressure changes in such a microchannel under different split modes and the flow distribution under different differential pressures. In order to improve the two-phase flow distribution uniformity, an optimization scheme of controlling the outlet pressure of branches is proposed and numerically analyzed. The results indicate a strong bidirectional coupling effect between the outlet pressure and the mass flow rate in the branches. Through optimizations, the value of $NSTD_l$ of this model can be reduced from 0.52 to 0.26. The main findings are summarized as follows:

1. As the gas slug moves and splits in the liquid phase, the pressure in the channel shows a trend of periodic changes. For different gas slug splitting modes, the pressure changes are similar. That is, when the gas slug is about to split into daughter bubbles, the pressure in the channel drops sharply and pressure fluctuations appear. For B_1 and B_2 modes, a sudden increase in pressure can be observed due to the gas slug blocking the main channel, but for B_3 and NB/B modes, there is no such phenomenon. Among them, NB/B mode shows a completely different pressure trend from the other three separation modes.

2. The differential pressure of each branch channel directly affects the flow distribution in the microchannel. By controlling the branch pressure, different flow distributions can be obtained. If the differential pressure of branch channel 1 is changed separately, the maldistribution phenomenon of the whole model can be optimized to some extent. The $NSTD_l$ value of the model decreases from 0.52 to 0.30. However, changing the differential pressure of branch channel 2 alone will make the maldistribution phenomenon more obvious which means that the flow difference between the three branch channels will be further increased.

3. The special elongated bubble structure formed during the gas slug splitting process helps the liquid phase enter the branch channel. When the flow state of a branch channel changes from two-phase flow to single-phase flow, the mass flow rate of the branch channel, with the change of differential pressure, has an obvious turning point.

4. When changing the differential pressure of branch channel 1, also changing the differential pressure of branch channel 2 appropriately to maintain branch channel 2 in a two-phase flow state can further minimise the maldistribution phenomenon of the whole model. The optimum $NSTD_l$ value was reduced from 0.52 to 0.26. In the actual application process, the same optimization effect can be achieved by changing the diameter of each branch channel.

Acknowledgments

This work is supported by the National Natural Science Foundation of China (No. 51976181).

Author contributions

Yu-qi HUANG designed the research. Peng-fei ZHANG processed the corresponding data and wrote the first draft of the manuscript. Yong-jun HUA helped to organize the manuscript. Xiang-guo XU revised and edited the manuscript.

Conflict of interest

Peng-fei ZHANG, Xiang-guo XU, Yong-jun HUA, and Yu-qi HUANG declare that they have no conflict of interest.

References

Asadolahi AN, Gupta R, Fletcher DF, et al., 2011. CFD approaches for the simulation of hydrodynamics and heat transfer in Taylor flow. *Chemical Engineering Science*, 66(22):5575-5584. https://doi.org/10.1016/j.ces.2011.07.047

Bao WD, 2019. Investigation on Battery Thermal Management System (BTMS) with Refrigerant-based Direct Cooling. MS Thesis, Jilin University, Changchun, China (in Chinese).

Bordbar A, Taassob A, Zarnaghsh A, et al., 2018. Slug flow in microchannels: numerical simulation and applications. *Journal of Industrial and Engineering Chemistry*, 62:26-39. https://doi.org/10.1016/j.jiec.2018.01.021

Chen JF, Wang SF, Cheng S, 2012. Experimental investigation of two-phase distribution in parallel micro-T channels under adiabatic condition. *Chemical Engineering Science*, 84:706-717. https://doi.org/10.1016/j.ces.2012.09.023

Dario ER, Tadrist L, Passos JC, 2013. Review on two-phase flow distribution in parallel channels with macro and micro hydraulic diameters: main results, analyses, trends. *Applied Thermal Engineering*, 59(1-2):316-335. https://doi.org/10.1016/j.applthermaleng.2013.04.060

Dario ER, Tadrist L, Oliveira JLG, et al., 2015. Measuring maldistribution of two-phase flows in multi-parallel microchannels. *Applied Thermal Engineering*, 91:924-937. https://doi.org/10.1016/j.applthermaleng.2015.08.103

Dong JX, Zhang XB, Wang FM, et al., 2018. Numerical study of phase split characteristics of slug flow at a branching micro-T-junction. *Asia-Pacific Journal of Chemical Engineering*, 13(4):e2213. https://doi.org/10.1002/apj.2213

Ferrari A, Magnini M, Thome JR, 2018. Numerical analysis of slug flow boiling in square microchannels. *International Journal of Heat and Mass Transfer*, 123:928-944. https://doi.org/10.1016/j.ijheatmasstransfer.2018.03.012

Giannetti N, Redo MA, Sholahudin, et al., 2020. Prediction of two-phase flow distribution in microchannel heat exchangers using artificial neural network. *International Journal of Refrigeration*, 111:53-62. https://doi.org/10.1016/j.ijrefrig.2019.11.028

Guo RW, Fu TT, Zhu CY, et al., 2020. Pressure drop model of gas-liquid flow with mass transfer in tree-typed microchannels. *Chemical Engineering Journal*, 397:125340. https://doi.org/10.1016/j.cej.2020.125340

He K, Wang SF, Huang JZ, 2011. The effect of surface tension on phase distribution of two-phase flow in a micro-T-junction. *Chemical Engineering Science*, 66(17):3962-3968. https://doi.org/10.1016/j.ces.2011.05.027

Hong SH, Tang YL, Wang SF, 2018. Investigation on critical heat flux of flow boiling in parallel microchannels with large aspect ratio: experimental and theoretical analysis. *International Journal of Heat and Mass Transfer*, 127:55-66. https://doi.org/10.1016/j.ijheatmasstransfer.2018.07.110

Hong SH, Jang DS, Park S, et al., 2020. Thermal performance of direct two-phase refrigerant cooling for lithium-ion batteries in electric vehicles. *Applied Thermal Engineering*, 173:115213. https://doi.org/10.1016/j.applthermaleng.2020.115213

Kim NH, Han SP, 2008. Distribution of air-water annular flow in a header of a parallel flow heat exchanger. *International Journal of Heat and Mass Transfer*, 51(5-6):977-992. https://doi.org/10.1016/j.ijheatmasstransfer.2007.05.028

Kim S, Lee SY, 2015. Split of two-phase plug flow with elongated bubbles at a microscale branching T-junction. *Chemical Engineering Science*, 134:119-128. https://doi.org/10.1016/j.ces.2015.04.020

Kumar R, Mithran N, Muniyandi V, 2017. Phase split in T-junction mini channel–a numerical study. *Chemical Product and Process Modeling*, 13(2):20170012. https://doi.org/10.1515/cppm-2017-0012

Lee WJ, Jeong JH, 2019. Development of a numerical analysis model for a multi-port mini-channel heat exchanger considering a two-phase flow distribution in the header. Part I: numerical modeling. *International Journal of Heat and Mass Transfer*, 138:1264-1280. https://doi.org/10.1016/j.ijheatmasstransfer.2019.04.100

Li HW, Li JW, Zhou YL, et al., 2017. Phase split characteristics of slug and annular flow in a dividing micro-T-junction. *Experimental Thermal and Fluid Science*, 80:244-258. https://doi.org/10.1016/j.expthermflusci.2016.08.024

Liang N, Shao SQ, Xu HB, et al., 2010. Instability of refrigeration system–a review. *Energy Conversion and Management*, 51(11):2169-2178. https://doi.org/10.1016/j.enconman.2010.03.010

Liu YC, Wang SF, 2019. Distribution of gas-liquid two-phase slug flow in parallel micro-channels with different branch spacing. *International Journal of Heat and Mass Transfer*, 132:606-617. https://doi.org/10.1016/j.ijheatmasstransfer.2018.12.040

Liu YC, Sun WC, Wang SF, 2017a. Experimental investigation of two-phase slug flow distribution in horizontal multi-parallel micro-channels. *Chemical Engineering Science*, 158:267-276. https://doi.org/10.1016/j.ces.2016.10.021

Liu YC, Sun WC, Wu W, et al., 2017b. Gas-liquid two-phase flow distribution in parallel micro-channels with different header and channels' orientations. *International Journal of Heat and Mass Transfer*, 112:767-778. https://doi.org/10.1016/j.ijheatmasstransfer.2017.05.029

Madanan U, Nayak R, Chatterjee D, et al., 2018. Experimental investigation on two-phase flow maldistribution in parallel minichannels with U-type configuration. *The Canadian Journal of Chemical Engineering*, 96(8):1820-1828. https://doi.org/10.1002/cjce.23112

Mahvi AJ, Garimella S, 2019a. Modeling framework to predict two-phase flow distribution in heat exchanger headers. *International Journal of Refrigeration*, 104:65-75. https://doi.org/10.1016/j.ijrefrig.2019.04.031

Mahvi AJ, Garimella S, 2019b. Two-phase flow distribution of saturated refrigerants in microchannel heat exchanger headers. *International Journal of Refrigeration*, 104:84-94.

https://doi.org/10.1016/j.ijrefrig.2019.04.026

Marchitto A, Fossa M, Guglielmini G, 2016. Phase split in parallel vertical channels in presence of a variable depth protrusion header. *Experimental Thermal and Fluid Science*, 74:257-264. https://doi.org/10.1016/j.expthermflusci.2015.12.017

Meinert H, Senger T, Wiebking N, et al., 2015. The plug-in hybrid technology of the new BMW X5 eDrive. *MTZ Worldwide*, 76(5):4-9. https://doi.org/10.1007/s38313-015-0004-z

Ménétrier-Deremble L, Tabeling P, 2006. Droplet breakup in microfluidic junctions of arbitrary angles. *Physical Review E*, 74(3):035303. https://doi.org/10.1103/PhysRevE.74.035303

Nie L, Wang MC, Zhao Y, 2020. Experimental study on direct refrigerant battery cooling system for electric vehicle. *Journal of Refrigeration*, 41(4):52-58 (in Chinese).

Redo MA, Jeong J, Giannetti N, et al., 2019. Characterization of two-phase flow distribution in microchannel heat exchanger header for air-conditioning system. *Experimental Thermal and Fluid Science*, 106:183-193. https://doi.org/10.1016/j.expthermflusci.2019.04.021

Roenby J, Bredmose H, Jasak H, 2016. A computational method for sharp interface advection. *Royal Society Open Science*, 3(11):160405. https://doi.org/10.1098/rsos.160405

Singh R, Bahga SS, Gupta A, 2020. Electrohydrodynamic droplet formation in a T-junction microfluidic device. *Journal of Fluid Mechanics*, 905:A29. https://doi.org/10.1017/jfm.2020.749

Tonomura O, Tanaka S, Noda M, et al., 2004. CFD-based optimal design of manifold in plate-fin microdevices. *Chemical Engineering Journal*, 101(1-3):397-402. https://doi.org/10.1016/j.cej.2003.10.022

Wang XD, Zhu CY, Fu TT, et al., 2014. Critical lengths for the transition of bubble breakup in microfluidic T-junctions. *Chemical Engineering Science*, 111:244-254. https://doi.org/10.1016/j.ces.2014.02.037

Yu W, Xu LY, Chen SJ, et al., 2019. Numerical study on flow boiling in a tree-shaped microchannel. *Fractals*, 27(7): 1950111. https://doi.org/10.1142/S0218348X19501111

Zhou M, Wang SF, Zhou Y, 2017. Phase distribution of nitrogen–water two-phase flow in parallel micro channels. *Heat and Mass Transfer*, 53(4):1175-1182. https://doi.org/10.1007/s00231-016-1884-4

Zou Y, Hrnjak PS, 2014. Effects of fluid properties on two-phase flow and refrigerant distribution in the vertical header of a reversible microchannel heat exchanger–comparing R245fa, R134a, R410A, and R32. *Applied Thermal Engineering*, 70(1):966-976. https://doi.org/10.1016/j.applthermaleng.2014.06.021